

Stacked-graphene layers as engineered solid-electrolyte interphase (SEI) grown by chemical vapour deposition for lithium-ion batteries

Taehoon Kim,^a Matthew R. Leyden,^a Luis K. Ono^a and Yabing Qi^{*,a}

Abstract

A multi-layer of stacked-graphene (8 layers of basal planes) grown by chemical vapour deposition (CVD) is introduced as an artificial solid electrolyte interphase (SEI) layer onto a transition metal oxide cathode for lithium-ion batteries. The basal planes are generally regarded as a strong physical barrier that prevents lithium-ion diffusion, although it is believed that a small number of lithium-ions can migrate through the defect sites of the stacked layers. Interestingly, the unique design of the stacked-graphene perpendicular to the basal planes not only effectively suppresses the formation of instable SEI layers, but also achieves a reasonable amount of battery charge capacities. To correctly understand the impact from the stacked design, we further studied the rate kinetics difference between slow cycles (0.125 C→0.250 C→0.400 C→0.125 C) and rapid cycles (C→2 C→3 C→C). We propose that the clap-net like design of the stacked-graphene could enable the effective conducting pathway for electron transport, while protecting the active material inside. The magnetic measurements reveal the efficient Li⁺ (de)intercalation into graphene-layers. The artificial SEI also renders the electrode/electrolyte interface more stable against dynamic rate changes. The present approach provides a particular advantage in developing high stability battery that can be utilized at various charge rates.

^a Energy Materials and Surface Sciences Unit (EMSSU), Okinawa Institute of Science and Technology Graduate University (OIST), 1919-1 Tancha, Onna-son, Okinawa 904-0495, Japan. * Corresponding author. TEL: +81-(0)98-966-8435 e-mail address: Yabing.Qi@OIST.jp (Y. B. Qi).

1. Introduction

Li-ion batteries have been widely used as an energy storage system for powering portable devices such as mobile phones and laptop computers since the successful commercialization by Sony in 1991 [1,2]. Recent developments in the batteries have led to a continuous interest in developing high energy density battery for electric vehicles (EV) and electrical grid applications owing to their high volumetric/gravimetric density, high energy density, flexible design, and environmentally benign property [1–6]. Certain advantages have allowed the expand of the energy storage system into more sophisticated applications that require a higher level of stability in service. One of the key components that determines the performance and stability of the battery is the type of intercalation compound [6,7]. The intercalation material, i.e., cathode can be categorized into three different types of composites based on the crystal structure, namely, spinel (LiMn_2O_4), olivine (LiMPO_4 , where $M=\text{Fe, Mn, Co, Ni}$), and layered transition metal oxides (LiMO_2 , where $M=\text{Mn, Co, Ni, Al}$) with distinguishing ionic diffusion channel [8–11]. Among the cathode materials, the layered structure has attracted much attention due to its successful commercialization with high specific capacity ($< 200 \text{ mAhg}^{-1}$) [2,8,12]. Further research on the battery chemistry of the layered oxide material had led to the development of the mixed transition metals oxide composite, i.e. $\text{LiNi}_x\text{Mn}_y\text{Co}_z\text{O}_2$ (NMC, where $x+y+z = 1$) with a $\alpha\text{-NaFeO}_2$ -structure ($R\bar{3}m$ space group). The NMC cathode has emerged as a promising electrode material as the mixed transition metals between Ni, Co, and Mn offer synergetic benefits over a single transition metal cathode [2,13–15]. A tailored NMC structure into a dual layer system, represented by the formula of $x\text{Li}_2\text{MnO}_3 \cdot (1-x)\text{LiMO}_2$ ($M=\text{Mn, Co, Ni}$), offers extra charge capacity. The electrode composite of the dual layer system is known as the Li-rich transition metal oxide cathode proposed by Thackeray et al [15]. The Li-rich battery benefits from its superior specific capacity ($\sim 250 \text{ mAhg}^{-1}$) and high operating voltage ($>4.6 \text{ V vs Li}^0$) [15–17]. Since then, interest in the Li-rich battery has dramatically increased, giving rise to the development of its derivatives such as ‘layered-layered-spinel’ electrode, Sn-stabilized Li-rich cathode, Al substituted Li-rich material, and Fe substituted Li-rich composite [18–21]. Recently, there has been a growing trend towards the development of layered Ni-rich oxide cathode due to its high energy density and promising reversible capacity [22]. While there have been extensive developments of the high-energy density materials, the adaptation of the fundamental layered structure remains unchanged, and thus some intrinsic problems causing battery fading are still present. The degradation of the two-

dimensional layered structure attributed to the formation of the solid-electrolyte interphase (SEI) layer is one of the fading mechanisms that lead to the charge capacity decrease, voltage decay, and power fading of the lithium-ion battery [23]. Electrode exfoliation, SEI growth and stabilization, and the subsequent lithium plating are known to be the dominant processes involved for the fading mechanism during charge-discharge [23]. On the one side, the formation of SEI layer is a critical factor, which causes the degradation of the electrode material and thus capacity fading. On the other side, it is also the key factor that provides the kinetic stability by preventing the redox reaction stemming from the electron transfer from higher to lower Fermi energy between electrode and electrolyte. The SEI layer also plays an important role in preventing the dissolution of the transition metal into the electrolyte and the oxygen loss from the active material [6,7,23,24]. The chemical and physical properties of the SEI on the battery electrodes have been widely studied. Previous studies on the SEI composition identified the formation of Li_2O , Li_2CO_3 , and LiF (e.g. LiPF_6 , LiBF_4 electrolyte) near the lithium metal substrate, whereas the major products at the electrolyte side were reported as alkyl carbonates, i.e. dicarbonates ($(\text{ROCO}_2\text{Li})_2$) and/or semicarbonates (ROCO_2Li) [25–28]. Based on the chemical compositions, Peled et al. proposed the mosaic-type SEI model to describe the formation and growth of the SEI layer during charge-discharge [25]. The SEI layer is considered as a mosaic consisting of multiple inorganic and organic components, allowing lithium ions to move through the phase boundaries. The mosaic model has been widely accepted, yet the detailed mechanism of SEI formation remains unclear.

Graphene has emerged as an attractive functional material for energy storage applications owing to its outstanding electrical conductivity ($\sim 2000 \text{ Scm}^{-1}$), large active surface area ($\sim 1500 \text{ m}^2\text{g}^{-1}$), high energy density and mechanical stability [29–34]. It has been also reported that the graphene can effectively inhibit the dissolution of the transition metals (e.g. Mn, Co, Ni) into the battery electrolyte [33,35,36]. Graphene not only hinders the side-reaction between the electrode and electrolyte, but also tends to increase the oxidation state of the transition metal, which in turn prevents the dissolution of the active material into the electrolyte during charge-discharge [35]. Another interesting feature of graphene is the ability of producing stable SEI layer on the electrode [37]. This feature called our attention to the concept of artificial SEI layer, which prevents the access of the electrolyte to the electrode and renders the surface chemically stabilized while it allows the migration of the lithium ions into the battery electrode [38–40]. The migration mechanism of the lithium-ions into the artificial SEI layer has become a central issue for the battery performance and rate capability. Several studies have explored

the lithium-ion intercalation into the graphite or stacked carbon nanostructures [29,41,42]. Recently, there has been a great interest in the stacked graphene system, which can be distinguished from the normal graphite, due to their unique electronic properties depending on the way of stacking and the number of graphene layers [43–47]. A particular interest is devoted to the lithium-ion diffusion through the basal plane [44,47]. Whereas the lithium-ion diffusion through the edge planes between graphene layers have been widely studied, the investigations of the lithium-ion diffusion through the basal plane are scarce as the perpendicular layer is generally regarded as a strong physical barrier that prevents the lithium-ion migration. However, a previous study by Yao et al. suggests the possible diffusion of lithium ions through the defect sites, i.e. grain boundaries and vacancies [44]. In addition, according to the layer-dependant capacities, it has been reported that higher than 6 graphene layers will reasonably increase the battery capacity by pure lithium ions intercalation [44]. Also, Persson et al. identified the grain boundary as a possible lithium-ion diffusion channel between stacked graphene layers [46].

In this study, we present an unique artificial SEI layer with 8 layers of stacked-graphene grown by chemical vapour deposition (CVD) and transferred onto the layered $\text{Li}(\text{Ni}_{1/3}\text{Mn}_{1/3}\text{Co}_{1/3})\text{O}_2$ cathode layer-by-layer. Kinetic investigations were conducted using different charge rate sets between slow cycles and rapid cycles of the lithium-ion cells to accurately evaluate the impact of the stacked graphene on the SEI formation and electrochemical properties. Lithium-ion diffusion through the defect sites of the stacked-graphene is confirmed. Interestingly, the stacked design perpendicular to the $\text{Li}(\text{Ni}_{1/3}\text{Mn}_{1/3}\text{Co}_{1/3})\text{O}_2$ electrode, not only effectively suppresses the formation of the SEI layer, but also provides a certain amount of charge capacity with improved rate capabilities. The clap-net like design of the stacked-graphene enables the effective conducting pathway for electron transportation achieving reasonable battery performance. Furthermore, it maintains the initial local atomic environments of Mn-O, Co-O, and Ni-O, impeding carbonates by-products. It also renders the interface stability against dynamic rate changes. This study provides insights into the development of high-energy density electrodes with enhanced stability for the lithium-ion battery.

2. Experimental

2.1. Graphene growth and transfer

Graphene was prepared first by cleaning copper foil (25 mm copper foil, Alfa Aesar), with dilute nitric acid (5%), followed by acetic acid, and lastly isopropyl alcohol. The foil was then loaded into a quartz tube furnace and ramped up to 1070 °C in the presence of hydrogen gas, and annealed for 1 hour. This was followed by a 30 min growth with a gas flow of 20 sccm hydrogen, and 30 sccm methane, and a pressure of ~200 Pa. The foil was then rapidly cooled to room temperature by opening the lid of the CVD system in the presence of hydrogen gas. Graphene was transferred to $\text{Li}(\text{Ni}_{1/3}\text{Mn}_{1/3}\text{Co}_{1/3})\text{O}_2$ electrode by a thermal release transfer process. Copper with graphene foil is covered with thermal release tape (Nitto, 90 °C release). The copper is etched away in solution of 20% ammonium persulphate, leaving 1 layer of graphene on the tape surface. Up to 8 layers were transferred sequentially (layer-by-layer) by first applying the tape with uniform pressure to battery substrates (denoted as GNP8L), followed by removal of the tape backing by heating the substrate to 100 °C. The synthesis process was performed inside a Class 1000 (ISO 6) clean room.

2.2. Electrode material characterization

The cycled coin cells were disassembled under argon atmosphere (Ar-glove box: $\text{H}_2\text{O} < 1$ ppm and $\text{O}_2 < 1$ ppm), and the cathodes cycled at different charge regimes were carefully taken and rinsed by DMC, followed by a drying process under vacuum, for the material characterizations. Magnetic measurements were conducted on the $\text{Li}(\text{Ni}_{1/3}\text{Mn}_{1/3}\text{Co}_{1/3})\text{O}_2$ (NMC111) and the stacked-graphene (8-layers) coated $\text{Li}(\text{Ni}_{1/3}\text{Mn}_{1/3}\text{Co}_{1/3})\text{O}_2$ cathodes (GNP8L) at different cycled states using a physical property measurement system (Quantum Design PPMS Dynacool). The magnetic susceptibility of the cathode composites was measured under the magnetic field of 30k Oe at 5 K. The molar magnetization property was also investigated by applying 1000 Oe magnetic field in the temperature range between 5 K and 300 K. SEM images of the cathodes (NMC111 and GNP8L) at reference state and cycled states were acquired by a scanning electron microscopy (SEM, FEI Quanta 250 FEG). The powder diffraction data of the cathodes with the different cycled conditions were collected using Bruker D8 X-ray diffractometer with the X-ray source of Cu $K\alpha$ radiation. The XRD peaks were recorded by step scanning in the range of $2\theta = 10-90^\circ$ with the increment of 0.02° . Raman spectra were

collected by a 3D laser Raman micro-spectrometer (Nanofinder 30, Tokyo Instruments). Raman investigation was conducted for 5 different points for each sample using a 532 nm excitation laser (green laser, spot size $\sim 2 \mu\text{m}$) with 50x objective lens (Nikon), and 600 grooves/mm grating. X-ray photoelectron spectroscopy (XPS, AXIS Ultra HSA KRATOS) was performed for the ex-situ study of the cathode materials at different rate regimes. Al $K\alpha$ was used as the X-ray source, and it was operated at 10 kV and 160 W under ultra-high vacuum (10^{-9} torr). The background of the spectra was fitted using a Shirley-type function. The spectra profiles were defined by a Gaussian-Lorentzian function using CasaXPS application.

2.3. Electrochemical characterization

NMC111 electrodes were prepared by mixing the $\text{Li}(\text{Ni}_{1/3}\text{Mn}_{1/3}\text{Co}_{1/3})\text{O}_2$ active material (MTI, Japan) with carbon black (Super C65) and polyvinylidene fluoride (PVDF) binder in a weight ratio of 80:10:10 (=NMC111:Carbon black:PVDF) in N-methyl-2-pyrrolidone (NMP, Sigma Aldrich) solution. GNP8L electrodes were produced by the thermal-realising taping method of graphene on the as-prepared NMC111 electrodes. The electrode slurries were coated on the aluminium current-collector using an electrode coater equipped with a doctor blade and a dryer (MTI, Japan), and the casted film was dried at 60°C for overnight. The casted electrodes were taken into the vacuum oven and dried at 120°C for another overnight. The casted electrodes were roll-pressed with $10 \mu\text{m}$ thickness after the vacuum drying, and transferred into an Ar-glove box in order to assemble the electrode components into a CR2032 coin cell type. Prior to assembling, the electrodes were cut into a piece of discs to 16 mm in diameter. Li metal was used as the counter electrode (anode), and it was cut into the same diameter size as the cathode. The cathode and anode were physically separated by a membrane separator (CELGARD Inc.). 1 M lithium hexafluorophosphate (LiPF_6) in ethylcarbonate (EC), diethylcarbonate (DC), and dimethylcarbonate (DMC) (EC:DC:DMC = 1:1:1 in volume) was used as the electrolyte. A stainless steel spacer and a steel spring were put on top of the anode, and they were sealed by a hydraulic crimping machine (MTI, MSK-110). The assembled coin cells were charged and discharged with the current rate of 1 C, 2 C, 3 C, and back to 1 C (denoted as rapid charge regime), and the cells were charged and discharged with the current rate of 0.125 C, 0.250 C, 0.400 C, and back to 0.125 C (denoted as slow charge regime) using an 8-channel battery analyser (MTI). The galvanostatic profile was obtained in the voltage range of 2.0 – 4.2 V at room temperature with 40 cycles for each cell.

3. Result and discussion

Magnetism studies are particularly useful in understanding the local atomic environment of the $\text{Li}(\text{Ni}_{1/3}\text{Mn}_{1/3}\text{Co}_{1/3})\text{O}_2$ cathode composite and providing insights into the graphene defects and charge rate kinetic of the stacked-graphene $\text{Li}(\text{Ni}_{1/3}\text{Mn}_{1/3}\text{Co}_{1/3})\text{O}_2$ cathode (GNP8L). The Curie-Weiss temperature (θ), denoted as Weiss constant (Table. S1), from the magnetic susceptibility measurements can offer information on the type and strength of the magnetic exchanges. Especially, the identification of an antiferromagnetic exchange proves the presence of the 180° Ni-O-Ni interactions between the Li-layer and the transition metal layer in the electrode. In addition, the evaluation of the magnetic moment (μ_B) upon the number of graphene layers offers information about the occurrence of the graphene defects. Fig. 1a exhibits the schematics of the battery cathode coated by the stacked graphene with defect sites. The interactions appeared at the electrode interface on Li^+ charge rate kinetics is also displayed. It has been demonstrated that the graphene grown by the CVD method can well maintain the initial electron spin state along with a wide range of the substrate [48]. This feature is illustrated as the electrons with identical spin states onto the graphene layer. The green circle represents the individual lithium-ion and the orange arrow indicates the migration pathway. The different migration speed of Li^+ is likely to be attributed to the rate dependent intercalation mechanism [49]. Whereas the Li^+ migrates through the defect sites instantly at a rapid charge rate, the Li^+ possibly competes with other Li^+ and/or Li^+ based compounds (e.g. LiF , LiOH , and lithium carbonates) resulting from SEI dissolution into the electrolyte at a slow charge rate. The difference in the charge rate could determine the presence of the steric hindrance at the defect sites. Fig. 1b compares the performance of the electrochemical cells with the different number of graphene layers. GNP8L revealed the best charge capacity and rate capability except for the initial cycle. Further information on the electrochemical performance can be seen in Fig. S1 and Fig. S2. The magnetization and reciprocal magnetic susceptibility are compared in Fig. 1c–e. No saturation was found in the magnetization curve (Fig. 1e) for each sample, indicating antiferromagnetic interactions. As shown in Fig. 1c, the electrodes appear to be paramagnetic above 150 K, and thus the Curie-Weiss law of $X_m = C/(T - \theta)$, where C is the Curie constant ($C = N\mu^2/3k_B$, N : Avogadro number, μ : effective moment and k_B : Boltzmann constant) and θ is the Weiss constant, can be applied with the linear fitting between 150 K and 300 K. The Curie-Weiss temperature for the NMC111-REF, GNP2L-REF, GNP8L-REF, GNP8L-Rapid,

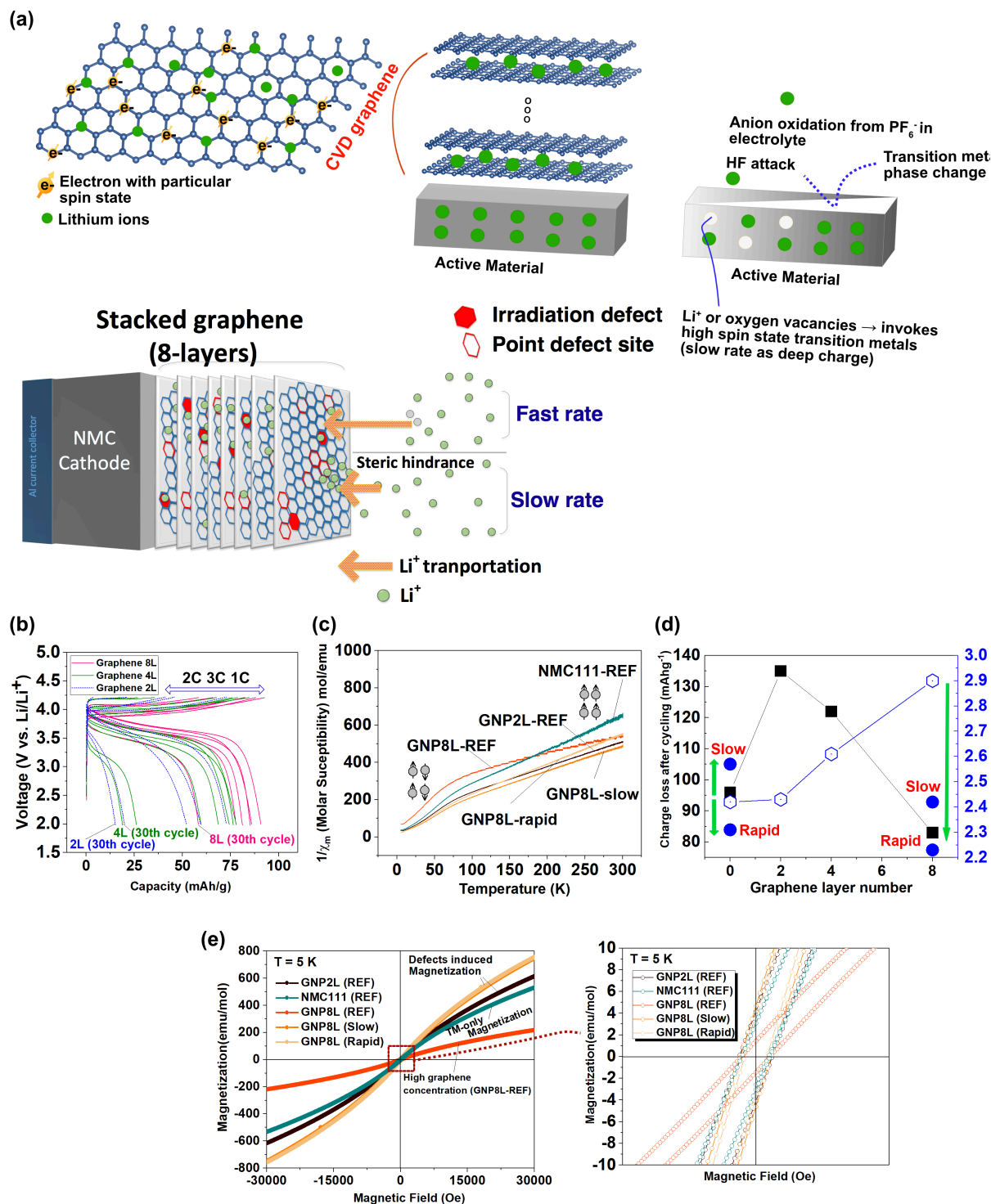


Fig. 1. (a) Schematics of stacked-graphene coating on the Li(Ni_{1/3}Mn_{1/3}Co_{1/3})O₂ (NMC) cathode, and difference in the charge rate kinetic at graphene defect sites and the electrode interface. (b) Galvanostatic profile of 2-layers stacked graphene NMC (GNP2L), 4-layers stacked graphene NMC (GNP4L), and 8-layers stacked graphene (GNP-8L), and their (c) reciprocal magnetic susceptibility between 5 K and 300 K. The applied magnetic field is 1000 Oe. (d) The correlation of experimental magnetic moments and charge losses after cycling on the number of stacked-graphene layers. Green arrow indicates the magnetic moment changes after cycling (e) Hysteresis loop of magnetization at 5 K of Li(Ni_{1/3}Mn_{1/3}Co_{1/3})O₂ (NMC) reference cathode, GNP2L at reference, GNP8L at reference, 8-layers stacked graphene NMC with rapid cycles (GNP8L Rapid) from C to 2 C to 3 C and back to C rate, and 8-layers stacked graphene NMC with slow cycles (GNP8L Slow) from 0.125 C to 0.250 C to 0.400 C and back to 0.125 C.

and GNP8L-Slow were evaluated to be -76.32 K, -79.98 K, -280.40 K, -44.18 K, and -62.74 K, respectively (detailed information on magnetization is summarized in Table S1). The

negative values of the Curie-Weiss temperatures further support the antiferromagnetic interactions. The origin of the antiferromagnetic interactions can be explained by the presence of Ni^{2+} in the lithium layer of the $\text{Li}(\text{Ni}_{1/3}\text{Mn}_{1/3}\text{Co}_{1/3})\text{O}_2$ cathode as it induces a 180° antiferromagnetic interaction with the Ni^{2+} in the transition metal layer [50–52]. Slight hysteresis loops could be observed for each electrode as can be seen in Fig. 1b. The remnant magnetization of NMC111 (REF) was measured to be $3.08 \text{ emu}\cdot\text{mol}^{-1}$. The remnant magnetization was $4.16 \text{ emu}\cdot\text{mol}^{-1}$ for the GNP2L (REF) cathode and was $1.45 \text{ emu}\cdot\text{mol}^{-1}$ for the GNP8L (REF) cathode. After the electrochemical cycles, the remnant magnetizations increased from $1.45 \text{ emu}\cdot\text{mol}^{-1}$ to $3.64 \text{ emu}\cdot\text{mol}^{-1}$ and to $4.66 \text{ emu}\cdot\text{mol}^{-1}$ for the slowly cycled GNP8L and rapidly cycled GNP8L, respectively. The slight opening of the magnetization curve is associated with a 180° ferromagnetic interaction between the Ni^{2+} in the lithium layer and Mn^{4+} in the transition metal layer [51–53]. These results signify larger changes in the local atomic environment of the stacked-graphene cell at slow charge rates. Another significant finding that can be deduced from the magnetic measurement is the magnetic behaviour of the stacked graphene itself. Defect induced magnetization by graphene could be identified in Fig. 1d, e. The magnetic behaviour in NMC111 electrode can be described by the transition-metal only (TM-only) magnetization since the cathode is mainly composed of Mn^{4+} , low-spin Mn^{3+} , Co^{3+} , and Ni^{2+} . The coating of 2-layers stacked graphene is likely to add some magnetic moments due to the defect induced magnetization by graphene. The experimental magnetic moment resulting from the defects tends to increase with the increment of the graphene layers (see Fig. 1d). However, the magnetization (emu/mol) declines when the number of graphene layers increases higher than 6-layers (see Fig. S3). These findings are in agreement with a number of previous studies, which have explored the defect induced magnetism in graphene [54–57]. It has been reported that defects such as adatoms and/or vacancies can be present in graphene [44,54,56]. A magnetism study of graphene by Nair et al. reported the relationship between the magnetic property and the defect concentration based on point defects [57]. The magnetic moment is likely to be high per unit defect at very low concentrations of point defects, whereas the magnetic moment dramatically decreases at a certain level of the defect concentration. It should be also noted that those defects allow the transportation of lithium ions into the electrode in spite of the high diffusion barrier from the stacked layers [35,44]. The (de)intercalation of lithium ions to the active material is believed to lead to higher graphene defects.[58] The increase of the magnetization (emu/mol) at both cycled cells (GNP8L(Slow) and GNP8L (Rapid)) indicates a rise in the number of the defects. The magnetic moment of the

NMC111 electrode increased from 2.42 μ_B to 2.57 μ_B at the slow charge regime, while it declined to 2.31 μ_B at the rapid charge regime. On the other hand, the magnetic moment of GNP8L decreased from 2.90 μ_B to 2.42 μ_B and 2.23 μ_B for the slow charge regime and rapid charge regime, respectively. This discrepancy is attributed to the engineered electrode interface rendered by the stacked-graphene layers. The $\text{Li}(\text{Ni}_{1/3}\text{Mn}_{1/3}\text{Co}_{1/3})\text{O}_2$ cathode without any surface treatment can be easily oxidized by the electrolyte (PF_6^-), leading to the oxidation changes in the transition metals. The HF compound stemming from the residual water is another critical factor that can dissolve the transition metals. These surface interactions lead to the local atomic phase changes in the transition metal elements, thereby forming low-spin transition metals. The decline of the magnetic moment of NMC111 electrode at the rapid charge regime can be explained by the occurrence of the low-spin transition metals. On the other side, lithium ion vacancies or oxygen vacancies can be formed through the transition metal migration and the loss of lithium ions during charge-discharge. The lower the charge rate is, the deeper the Li^+ (de)intercalation is. It thus results in the formation of a larger number of vacancies that could invoke high-spin transition metals, leading to higher magnetic moments. By contrast, the drop in the magnetic moment of GNP8L at both charge regimes could be explained by the Li^+ intercalation either into layers or on defect sites. The charge loss after electrochemical cycles is also correlated to the number of stacked-graphene layer and the magnetic moment of the electrode, as presented in Fig. 1d. The charge loss was minimum for the GNP8L cell on cycling. The electrode coated with 2-layers and 4-layers of graphene revealed higher charge capacity loss after cycling. This result supports the concept of the corrosion-SEI dominant regime, which is discerned in accordance with the number of graphene layers [44].

The rate kinetic study was conducted to gain insights into the electrochemical performance and stability of the cathode with the stacked-graphene system. Two distinguishable regimes of charge rates were applied in order to reproduce some harsh environments at the electrode/electrolyte interface stemming from the lithium-ion (de)intercalation. Fig. 2 presents the rate capability (Fig. 2a and b) and the galvanostatic profile of NMC111 and GNP8L (Graphene 8L) samples with the variations of charge rates between C, 2C, and 3C at the rapid-charge regime and 0.125 C, 0.250C, and 0.4 C at the slow-charge regime. Whereas the change in the specific charge capacity was not significant at the slow-charge regime, there was a notable difference at the rapid-charge regime. Interestingly, GNP8L (Graphene 8L) cell revealed better rate capability and capacity retention than those of NMC111

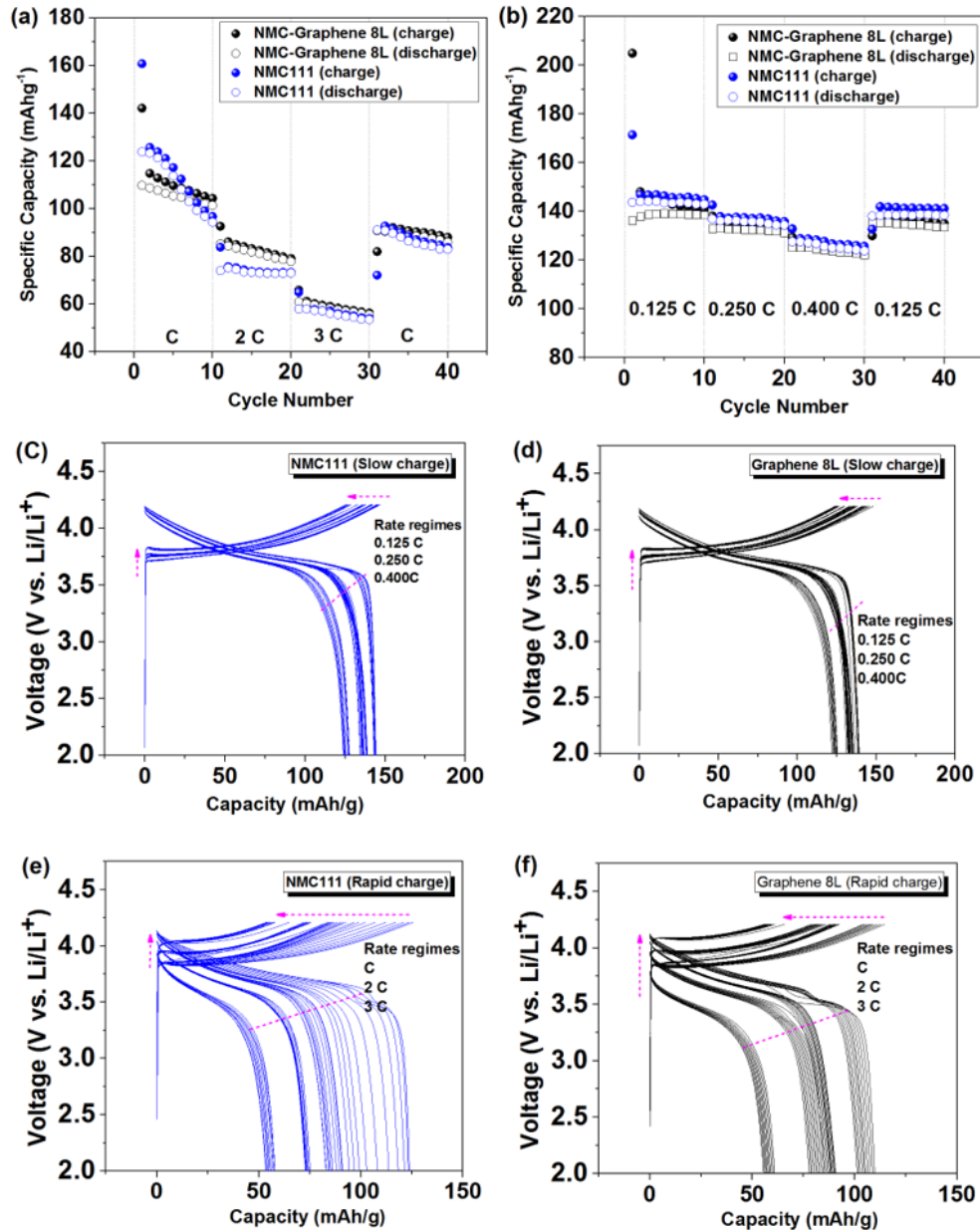


Fig. 2. Kinetics investigation of $\text{Li}(\text{Ni}_{1/3}\text{Mn}_{1/3}\text{Co}_{1/3})\text{O}_2$ (NMC111) and graphene coated NMC111 with 8 layers of stacked-graphene (Graphene 8L). Rate capability at (a) rapid charge regime (C, 2 C, 3C and C-rate) and (b) slow charge regime (0.125 C, 0.250 C, 0.400, and 0.125 C-rate). Galvanostatic profile of (c) NMC111 and (d) Graphene 8L (GNP8L) at slow charge regime in the voltage window of 4.2-2.0 V. Galvanostatic profile of (e) NMC111 and (f) Graphene 8L (GNP8L) at rapid charge regime in the voltage window of 4.2-2.0 V.

cell at the rapid-charge regime. Stacked graphene perpendicular to the substrate, known as the basal plane, has been generally considered as a physical barrier that blocks diffusion of lithium ions into the electrode substrate by steric hindrances [44,46]. Although ionic diffusion is highly limited between the stacked layers of graphene, some defect sites such as divacancies, ordered defects, and grain boundaries are likely to allow lithium ions to diffuse through the basal plane [44,46]. Also, it should be noted that the galvanostatic profile of GNP8L (Graphene 8L) cell

showed clearer separations in the rate regime compared to NMC111 cell at high charge rates (Fig. 2e and f), indicating better capacity retention and stability against dramatic changes in the ionic diffusion kinetic.

Fig. 3 compares the differential capacity obtained from initial, 9th, 15th, 25th, and 38th cycles of NMC111 and Graphene-8L (GNP8L) cells at the rapid charge regime with C, 2 C, 3 C, and C-rate applied and at the slow charge regime with 0.125 C, 0.250 C, 0.400 C, and 0.125 C-rate applied in the voltage window of 2.0 – 4.2 V. The initial peak location of NMC111 cell at around 3.8 V ascribed to $\text{Ni}^{2+}/\text{Ni}^{3+}/\text{Ni}^{4+}$ oxidation shifted to 3.74 V during the 0.125 C-rate cycling at the slow charge regime (Fig. 3a). There has been also an irreversible decrease in the peak intensity after the initial charge of NMC111 cell, implying phase changes in the local atomic environment of the cathode or/and the formation of SEI layer. The initial redox reaction of Graphene-8L (GNP8L) cell was found at around 3.8 V at a rate of 0.125 C, which is almost the same as in that of the NMC111 cell. By contrast, the intensity of the initial dQ/dV peak of Graphene-8L (GNP8L) showed a similar level to that on further cycles (Fig. 3b). On the other hand, the trend of spectrum shift at the rapid charge regime was similar between NMC111 and Graphene-8L (GNP8L) cells as shown in Fig. 3c and d. While there has been a notable difference in the intensity of the initial discharge, the location of the chemical potential attributed to the $\text{Ni}^{4+}/\text{Ni}^{3+}/\text{Ni}^{2+}$ reduction was similar regardless of the charge rate regime. Peak broadening and intensity decrease upon higher charge rates could be identified on both samples, indicating a continuous capacity fading. However, Graphene-8L (GNP8L) appeared to be more durable against charge variations that could lead to the formation of unstable SEI layers. Particularly, at the rapid charge regime, Graphene-8L (GNP8L) not only exhibited a higher peak intensity, but also better stability showing less changes in the redox voltage levels. The voltage difference of the redox reaction between C and 3 C-rate was 0.06 V for NMC111 and 0.01 V for Graphene-8L (GNP8L). The present observations on the electrochemical behaviour of the lithium ion cells are significant in two aspects. Firstly, it is surprising that the cells with stacked-graphene layers revealed better performance in the charge compensation process as compared to NMC111 cell. The fully covered electrode with 8 layers of graphene would be nonideal for lithium-ion diffusion, but they can still migrate through site defects. It has been also known that graphene synthesized on copper foil by chemical vapor deposition (CVD) introduces a homogeneous distribution of defects [59]. The key factor for delivering better charge capacity is possibly due to the functional design of the stacked layers, which mimics a pile of clap-net that is likely to be beneficial for collecting electrons from the intercalated

lithium ions (Fig. 1a). Secondly, the observations further support the concept of the rate-dependent intercalation pathway [49]. The discrepancy in the electrochemical behaviour upon different rate regimes can be explained by the inhomogeneous phase transformation that depends on the charge rates [49]. At a slow charge rate, the phase transformation of the active material particles tends to be homogenous, whereas the phase transformation at a rapid charge rate appears to be inhomogeneous as only particular particles are involved in the lithiation. Consequently, the lithium-ion at a higher charge rate is more likely than the lithium-ion at a lower charge rate to (de)intercalate in the cathode through the site defects or grain boundaries of the stacked graphene. This explains the relatively higher battery performance of Graphene-8L (GNP8L) as compared with NMC111 at the rapid charge regime.

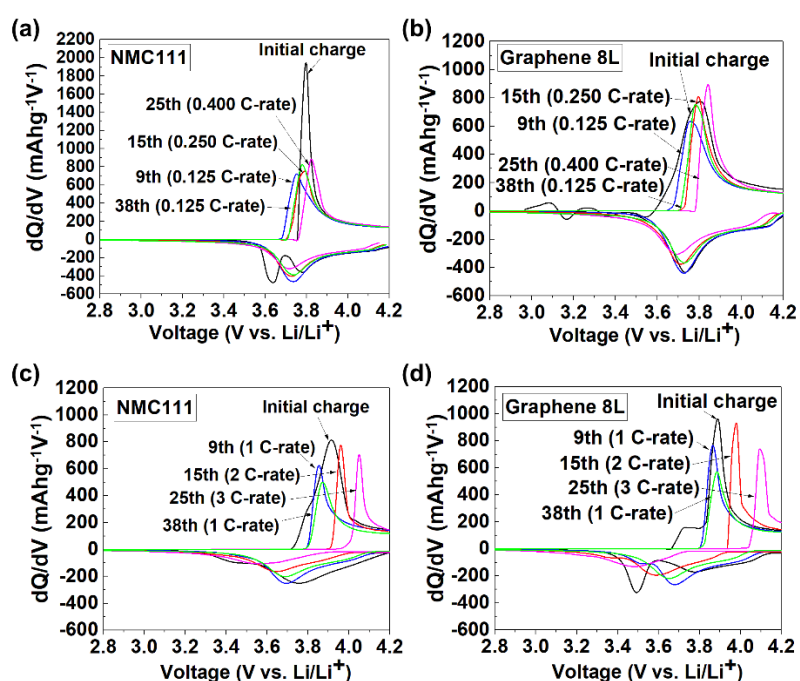


Fig. 3. dQ/dV plot vs cell voltage profile between initial and 40th cycle: (a) NMC111 at slow charge regime, (b) Graphene-8L (GNP8L) at slow charge regime, (c) NMC111 at rapid charge regime, and (d) Graphene-8L (GNP8L) at rapid charge regime.

Fig. 4a and b shows the SEM images of NMC111 and GNP8L cathodes at the reference state where no current was applied, and the observations on cycled cathodes at rapid and slow charge regimes. It can be seen from the SEM images that NMC111 underwent disruptions of the conductive additives or binding material, and dissolution of the active material particles after charge-discharge. By contrast, the stacked-graphene coated samples (GNP8L) revealed a well-preserved coating condition. The X-ray diffraction patterns are compared in Fig. 5a. Both NMC111 and GNP8L could be indexed by the LiMO_2 (trigonal, $R\bar{3}m$) structure, where $M = \text{Mn, Ni, and Co}$. Each of two coin cells for the sample type and the corresponding states were

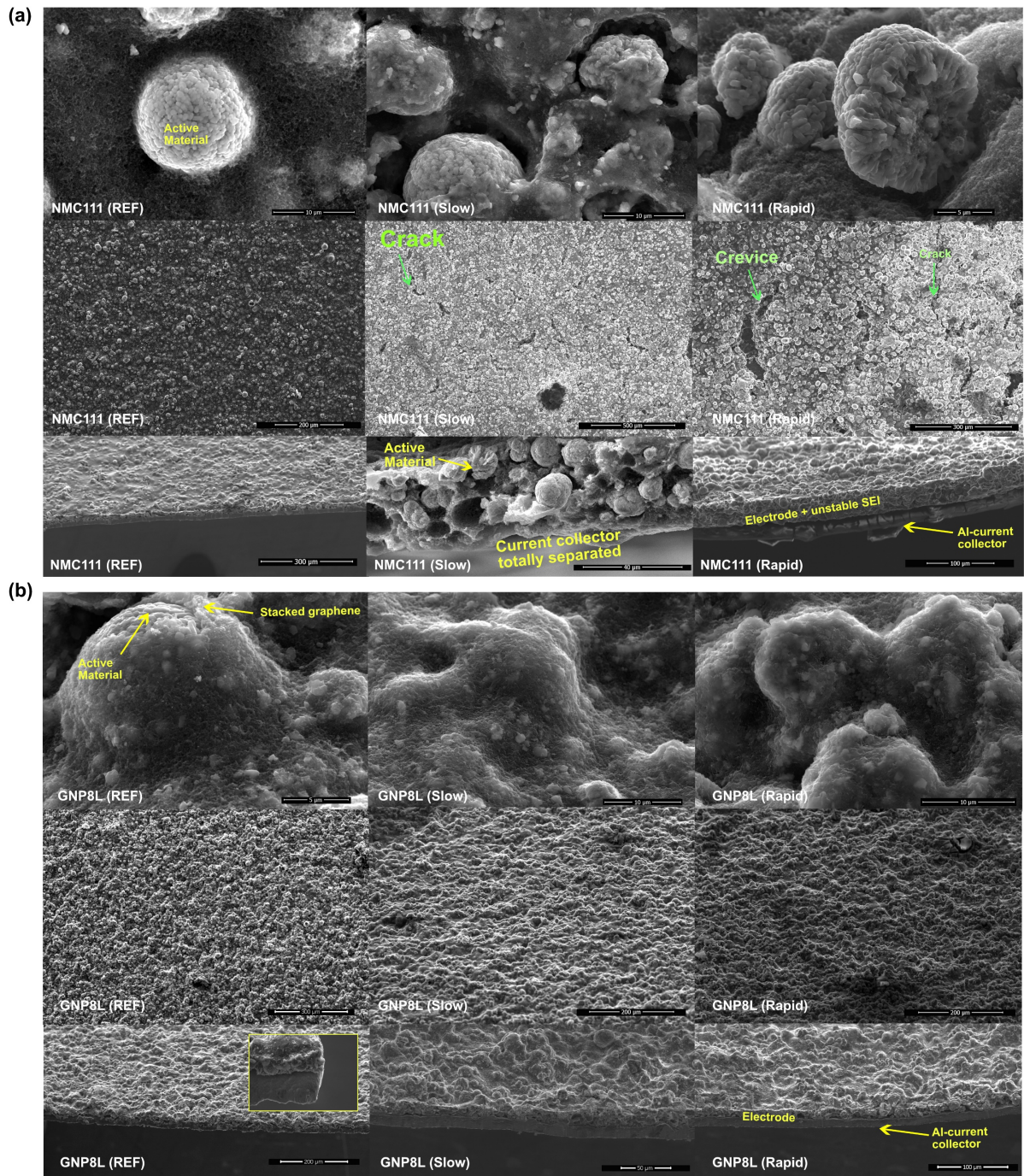


Fig. 4 SEM images of (a) NMC111 cathode at reference state (REF) where no current was applied, and at slow rate regime (NMC111(Slow)) and rapid rate regime (NMC111(Rapid)). SEM images of (b) GNP8L cathode at reference state (REF) where no current was applied, and at slow rate regime (GNP8L(Slow)) and rapid rate regime (GNP8L(Rapid)). (c) Comparison of powder diffraction patterns between NMC111 and GNP8L cathodes. The cells at the rapid charge regime were cycled at C, 2 C, 3C and C-rate, while the cells at the slow charge regime were cycled at 0.125 C, 0.250 C, 0.400, and 0.125 C-rate in the voltage window of 4.2 – 2.0 V.

prepared. NMC111 showed a notable change in the peak intensity at (003). While the peak increased after rapid cycles, the peak dramatically decreased after slow charge-discharge of NMC111 cells. There has been also a marked change in the peak intensity at (101), (104) and

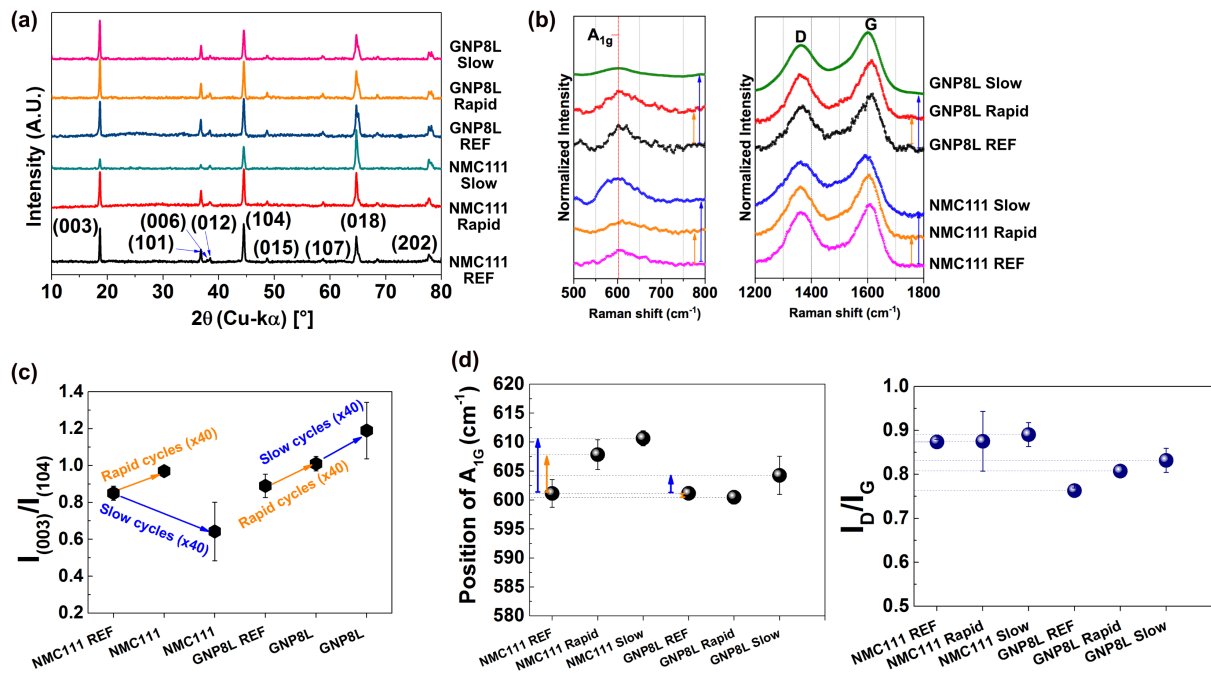


Fig. 5 Comparison of powder diffraction patterns between (a) NMC111 and GNP8L cathodes. (b) Key Raman spectra (A_{1g} , D-band, and G-band) of NMC111 and GNP8L at reference state, slow charge regime, and rapid charge regime. (c) Comparison of the XRD intensity ratio changes of $I(003)/I(004)$ between NMC111 and GNP8L. (d) The location change of Raman A_{1g} mode on different charge rate regimes between NMC111 and GNP8L. The blue arrow represents the slow cycle regime, while the orange arrow indicates the rapid cycle regime. Raman intensity change of D-band/G-band on different charge regimes. The cells at the rapid charge regime were cycled at C, 2 C, 3C and C-rate, while the cells at the slow charge regime were cycled at 0.125 C, 0.250 C, 0.400, and 0.125 C-rate in the voltage window of 4.2 – 2.0 V.

(108). Especially, after the slow cycles, the peak intensity of NMC111 at (101) declined substantially. By contrast, the peak intensity of GNP8L at (003) was similar between rapid and slow cycles. Also, there have been little change in the peak intensity at (101) for GNP8L after the electrochemical cycles. The peaks at (101) and (104) are generally considered as an indication of the successful lithium-ion (de)intercalation [60]. The decrease in the intensity at those peaks represent the loss of lithium-ions of NMC111 cathode during charge-discharge, implying a phase transition in the crystallography structure. In addition, the variations in the peak intensity at (108) of NMC111 indicate the structural distortion in the layered structure of the trigonal phase ($R\bar{3}m$) [61]. The coated cells with stacked-graphene (GNP8L) displayed significantly improved stability to the substrate structure on charge rate variations. To further understand the local atomic environment in the layered structure, the intensity ratio of diffraction peaks between (003) and (104) was evaluated as can be seen in Fig. 5c. The peak intensity of I_{003}/I_{104} is known to be associated with the Ni^{2+} cation mixing at the lithium-layer site. The higher the value of I_{003}/I_{104} is, the lower cation mixing between Ni^{2+} and Li^+ at the lithium-layer is [62,63]. It can be seen from the trend of I_{003}/I_{104} that the Ni^{2+} at the lithium-

layer is likely to be diminished during Li^+ (de)intercalation at rapid charge rates on both NMC111 and GNP8L cells. However, the peak intensity of I_{003}/I_{104} decreased in the slow charge regime of NMC111 cell, implying increment in the cationic disorder. Interestingly, the peak intensity of I_{003}/I_{104} in the rapid charge regime of GNP8L cell was rather increased. This signifies a well-ordered layered structure in GNP8L cathode even after the severe electrochemical cycles. The results obtained from the Raman spectroscopy are compared in Fig. 5b. Raman spectroscopy provides key information about the local atomic structure of the MO_6 octahedron (M=Transition metal). It also offers some insights into the carbon or graphitic system due to the high sensitivity of Raman scattering (D-band and G-band) to the distortion in the sp^2 carbon atoms. The Raman mode of A_{1g} is attributed to the M-O stretching, and it represents the order in the layered structure of hexagonal rock-salt system. The A_{1g} mode was located at approximately 600 cm^{-1} for both NMC111 and GNP8L cathodes at the reference state (REF). After rapid cycles, the A_{1g} of NMC111 shifted towards a higher frequency, but no significant change was observed in GNP8L (GNP8L Rapid), as exhibited in Fig. 5d. After slow cycles, the location of A_{1g} shifted towards a higher frequency as 611 cm^{-1} for NMC111 and 604 cm^{-1} for GNP8L. At both charge regimes, GNP8L revealed better stability, and these results are in good agreement with the powder diffraction measurements. It seems that those cells cycled at the slow charge regime could fully activate the redox reactions for the charge compensation mechanism, which in turn results in higher charge capacity as shown in Fig. 2. On the other hand, at the rapid charge regime, the obtained capacity was relatively lower than that of the slow charge regime, although it reached the target voltage quicker. At constant current cycles, the slow charge rate generally exerts higher impact on the underlying structure due to the fully activated/oxidized active materials, which leads to high battery capacity. The stacked-graphene coating on the $\text{Li}(\text{Ni}_{1/3}\text{Mn}_{1/3}\text{Co}_{1/3})\text{O}_2$ cathode appears to be stable under the cycling condition, i.e., dynamic changes of charge-discharge rates. The tendency could be also found in the Raman D-band and G-band of the cathode materials. The ratio of Raman peak intensity I_D/I_G can be used as an indicator to evaluate the defects in the carbon and graphitic system. The appearance of the G-band can be attributed to the plane stretching motion between sp^2 carbons, whereas the D-band is assigned to the structural defects (e.g. broken sp^2) and/or edge effects of the graphitic system [64–66]. The higher the value of I_D/I_G is, the more defects and disorders in the structure are [64,65]. It is difficult to directly compare the I_D/I_G ratio between NMC111 and GNP8L cathodes, due to the different origin of the carbonic system. However, there was an important difference in the value of I_D/I_G between the slow charge and rapid charge regime

as presented in Fig. 5b and d. The change of I_D/I_G was not significant for NMC111, but there was a notable increase in the value of I_D/I_G for GNP8L. The increment of the ratio was relatively large at the slow charge regime, indicating a higher degree of defects and disorders of the sp^2 carbon bonding. These results are consistent with the magnetic measurements on the defect-induced graphene upon different charge regimes (Fig. 1). Due to the steric hindrance, which is possibly originated from the rate-dependent (de)intercalation, the cathode cycled at slow charge rates may introduce relatively a larger number of defects on the stacked-graphene layers. The increase of disorders and defects (higher I_D/I_G) could diminish the electron conductivity, which in turn results in lower charge capacity [66,67]. This is in accord with the electrochemical measurements (Fig. 2). The formation of graphene layers identified by Raman 2D-band can be seen in Fig. S4.

The chemical property of the electrode materials was examined using XPS to evaluate the oxidation states of the transition metals, as well as to compare the SEI formation on the electrode upon different charge rates. Fig. 6 presents the XPS spectra of NMC111 and GNP8L at Mn 2p, Ni 2p, O 1s, C 1s, and F 1s between the slow and rapid charge regimes. The binding energy values of Mn ($2p_{3/2}$) and Mn ($2p_{1/2}$) were approximately 642.3 eV and 654.0 eV at the reference state (REF), respectively, indicating the presence of Mn^{4+} on both samples [68]. On the other side, the peaks at 641.7 eV and 653.3 eV imply the existence of some Mn^{3+} in the cathode at the reference state as can be seen in Fig. 6a and d [69]. It is likely that the Mn in the pristine material exists as a mixed oxidation state between Mn^{3+} and Mn^{4+} . This can be explained by the presence of low-spin Mn^{3+} and/or the electron transfer between Mn^{4+} and Ni^{2+} [70–72]. The spectral shift on both cells towards higher oxidation state in Mn 2p was only marginal at the rapid charge regime. However, at the slow charge regime, the shift was dramatic in NMC111 cell as it shifted from 642.3 eV to 645.2 eV while the change remained insignificant in GNP8L cell. This observation indicates the irreversible loss of the Mn of which its oxidation state lies between Mn^{3+} and Mn^{4+} from NMC111 cathode in the slow charge regime. The Ni ($2p_{3/2}$) and Ni ($2p_{1/2}$) peaks were identified at 854.5 eV and 872.1 eV followed by shake-up peaks (satellites) at approximately 860.9 eV and 879.0 eV (Fig. 6b and e), respectively, suggesting the existence of Ni^{2+} in the pristine composite. There were also two minor peaks at approximately 855.9 eV and 874.0 eV attributed to the Ni^{3+} . The occurrence of the minor peaks can be also caused by electron transfer between Mn^{4+} and Ni^{2+} . The trend of the XPS spectral shift of Ni 2p is comparable to that of the Mn 2p on both GNP8L and NMC111 cathodes on charge-discharge. As to NMC111 cell, the oxidation state change of Ni 2p was prominent at

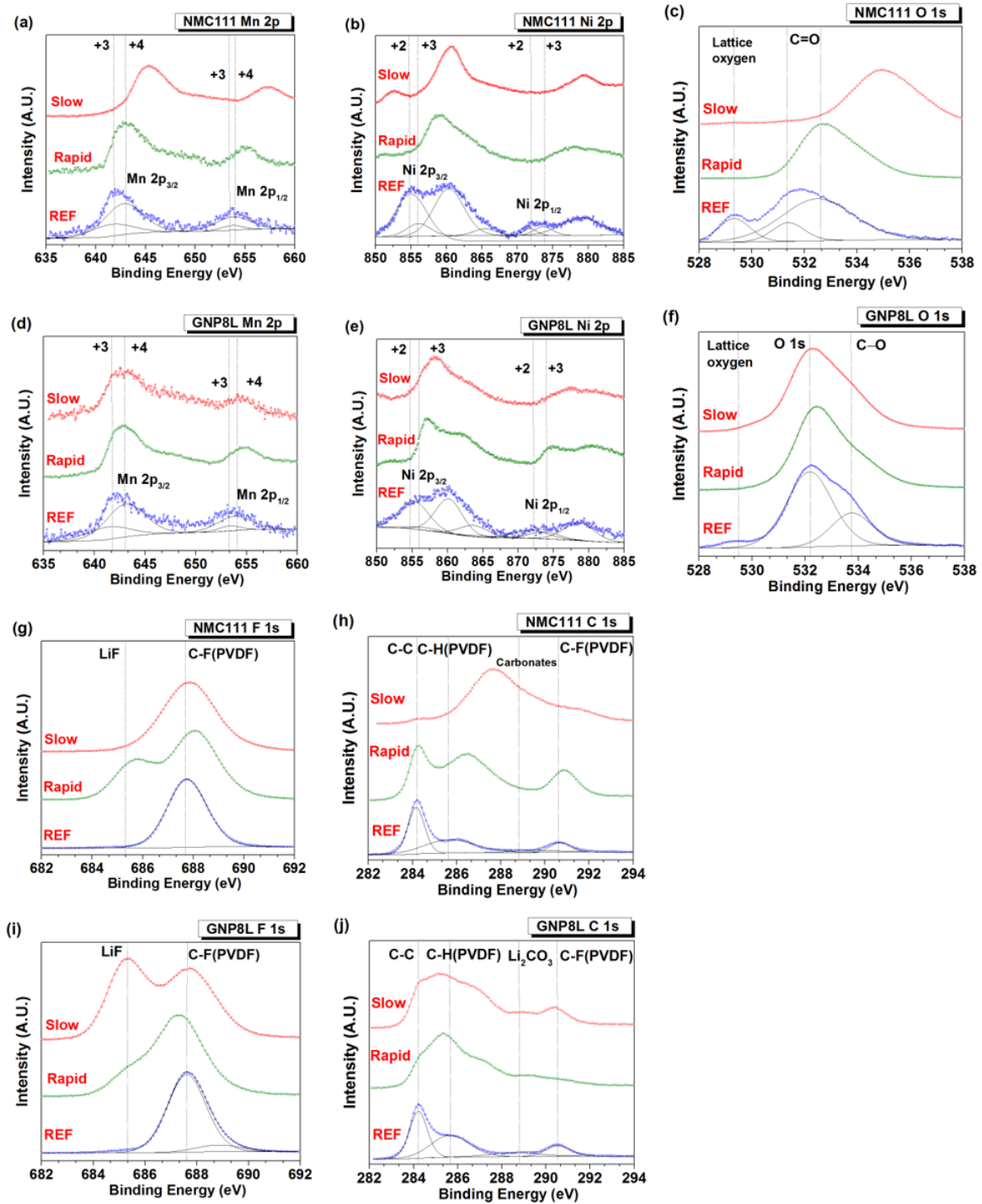


Fig. 6 XPS spectra of NMC111 sample: (a) Mn 2p, (b) Ni 2p, and (c) O 1s at reference state (REF), slow charge regime from 0.125 C to 0.250 C to 0.400 C (Slow) and back to 0.125 C, and rapid charge regime from C to 2 C to 3 C and back to C (Rapid). XPS spectra of GNP8L sample: (d) Mn 2p, (e) Ni 2p, and (f) O 1s at reference state (REF), slow charge regime from 0.125 C to 0.250 C to 0.400 C (Slow) and back to 0.125 C, and rapid charge regime from C to 2 C to 3 C and back to C (Rapid). XPS spectra of NMC111 sample: (g) F 1s and (h) C 1s at reference state (REF), slow charge regime from 0.125 C to 0.250 C to 0.400 C (Slow) and back to 0.125 C, and rapid charge regime from C to 2 C to 3 C and back to C (Rapid). XPS spectra of GNP8L sample: (j) F 1s and (i) C 1s at reference state (REF), slow charge regime from 0.125 C to 0.250 C to 0.400 C (Slow) and back to 0.125 C, and rapid charge regime from C to 2 C to 3 C and back to C (Rapid).

slow charge rates, and this tendency was similar to that of Mn 2p. However, the spectral shift of Ni 2p was also notable at rapid charge rates as it shifted from 854.5 eV to 858.9 eV (Fig. 6b)

after 40 cycles. On the other hand, the spectral changes of Ni 2p were relatively small in GNP8L cell as shown in Fig. 6e. It is likely that the Ni in GNP8L cell underwent less phase transition and/or less dissolution into the electrolyte upon charge-discharge. Ni is generally known as the major contributor to the charge compensation mechanism due to its two-stage oxidation of $\text{Ni}^{2+}/\text{Ni}^{3+}$ and $\text{Ni}^{3+}/\text{Ni}^{4+}$ during charge-discharge. Moreover, Ni is also relevant to the cation exchange between Li and Ni at the layered structure, and thus affects the ionic diffusion rate. As a consequence, the complex manner of the Ni in the cathode composite gives dynamic spectral changes upon different cycling conditions. Similarly to Ni 2p, there was a major binding energy shift in Mn 2p at the slow charge regime of NMC111. This result could be attributed to the oxidation state change from mixed $\text{Mn}^{3+}/\text{Mn}^{4+}$ to Mn^{4+} which contributes to the charge compensation mechanism. However, it is difficult to explain the major changes towards higher binding energy only by considering the irreversible oxidation change of Mn, since the electrons transferred are not sufficient to cause such a large spectral shift. The major reason for the spectral change of the Mn 2p in NMC111 might be due to the Mn dissolution from the electrode surface into the electrolyte during electrochemical cycling. It is believed that the trace amount of Mn^{3+} in the cathode triggers the acidic corrosion reaction with the HF stemming from the decomposition of LiPF_6 salt, as a consequence of residual water in the electrolyte [73,74]. Though the origin of the spectral shifts differs upon chemical species, it is the slow charge regime that reveals the higher binding energy shift after 40 cycles. There are two possible explanations for this result. As presented in the galvanostatic profile (Fig. 1a and b), the slow charge rates seem to fully activate the transport of electrons involved in the charge compensation mechanism, and thus results in higher charge capacity than the rapid charge rates. This in turn exerts a strong influence on the atomic phase transition of the transition metals. These findings are consistent with the results obtained from XRD and Raman spectroscopy. Another possible explanation is the rate-dependent phase transformation, as previously mentioned. At the rapid charge regime, either a fully intercalated or a fully deintercalated phase exists, whereas intermediate phases are likely to be present at the slow charge regime [49]. Hence, there will be larger spectral shifts at slow charge rates due to the coexistence between the fully oxidized transition metal and the larger amount of the intermediate phases. However, at both cases, GNP8L demonstrated its superior capability to protect the cathode material from its atomic phase transformation and dissolution into the electrolyte. The results obtained from the XPS analysis for O 1s are shown in Fig. 6c and f for NMC111 and GNP8L, respectively. The peak at approximately 529.3 eV is associated with the lattice oxygen (Mn-O, Co-O, and

Ni-O) in the cathode composite at the reference state [75]. The intensity of this peak was relatively low in GNP8L as compared with that in NMC111. This observation could be attributed to the coating of the stacked graphene with 8-layers, which in turn hinders the XPS beam penetration. There was also a smaller peak at approximately 531.3 eV in NMC111 at the reference state. The peak corresponds to Li_2CO_3 , which generally appears at the pristine state of the cathode material [75,76]. XPS O1s of GNP8L would be mainly described by another notable peak at approximately 532.2 eV (Fig. 6f), which can be assigned to the metallic carbonate (CO_3^{2-}) and the oxygen bond to graphene [75–77]. The appearance of the peak at 532.2 eV in GNP8L signifies a strong affinity between graphene and $\text{Li}(\text{Ni}_{1/3}\text{Mn}_{1/3}\text{Co}_{1/3})\text{O}_2$ composite [78]. There has been a notable change in the intensity and location of the O1s binding energy after the rapid cycles of NMC111 cells. The shifts towards a higher binding energy was dramatic at the rapid charge regime of NMC111 as can be seen in Fig. 6c. This observation accords with the XPS spectral shifts of the transition metals, and the charge kinetic appears to be more sensitive to the oxygen anions, which are believed to be evolved in the oxygen gas during charge-discharge [79,80]. By contrast, there has been little difference in the spectral shifts at O1s between the reference and cycled states of GNP8L cells, exhibiting considerable stability against oxygen loss, SEI formation from metal carbonates, and charge kinetics. Fig. 6g and i compare the XPS spectra obtained from the F 1s region on NMC111 and GNP8L cathodes. At the reference state (REF), where no current was applied, there was a peak at 687.7 eV that corresponds to the F from the PVDF binder and/or $\text{Li}_x\text{PO}_y\text{F}_z$ species on both cathodes [81,82]. After the rapid cycles, the F 1s of NMC111 contained a new peak close to 685.3 eV. The new peak can be assigned to the F species in LiF, which is one of the key components of SEI layer [37,81,83]. At the slow charge regime, the LiF peak did not occur in the F 1s of NMC111 sample. In contrast, as to GNP8L, the LiF peak at F 1s was observed at the slow charge regime, whereas it was not clear at the rapid charge regime. These intriguing observations raise questions about the nature of charge-dependent (de)intercalation of the lithium-ions. Homogenous and steady (de)intercalation at the slow charge regime is likely to result in less LiF formation in the SEI layer. Inhomogeneous and active (de)intercalation at the rapid charge regime tends to produce a higher amount of LiF on the electrode surface as a part of SEI layer. This can be simply explained by the vigorous decomposition of the LiPF_6 into LiF and Li_xPF_y at higher C-rates, and thus a higher amount of LiF will be formed on the $\text{Li}(\text{Ni}_{1/3}\text{Mn}_{1/3}\text{Co}_{1/3})\text{O}_2$ composite. However, a new surface environment originated from the stacking of 8 layers of graphene on the electrode possibly alters the way the LiF is formed

depending on charge rates. Graphene itself is believed to be very effective in forming a stabilized and well-defined SEI layer [37,44]. In addition, the structure of stacked graphene layers, commonly termed as the basal plane, is generally known to form a thinner SEI layer as compared with the edge plane [84]. The appearance of the LiF peak in the region of F 1s at the slow charge regime of GNP8L (Fig. 6i) could be attributed to the steric hindrance from the aggregated lithium-ions [44]. At fast charge rates, the native Li^+ will intercalate to the cathode composite rapidly passing through the defects and grain boundaries of the graphene layers. However, at slow charge rates, the native Li^+ may compete with the LiF component in the electrolyte, which in turn leads to the steric hindrance at the defect sites (Fig. 1a). The C1s XPS spectra consists of 284.2 eV, 285.6 eV, and 290.6 eV are shown in Fig. 6j for NMC111 and GNP8L cathodes, respectively. The first peak at approximately 284.2 eV can be assigned to the conductive carbon [78,85]. The second peak at 285.6 eV and the third peak at 290 eV are attributed to the PVDF binder [73,86]. After the rapid cycling of NMC111 cell, the C-H peak slightly increased and shifted towards higher binding energy indicating some chemical modifications in the PVDF binder. This is in accord with the spectral change of the C-F peak, also suggesting chemical changes in the PVDF binder after the rapid cycles of NMC111 cell. At the slow charge regime of NMC111, the C-H and C-F peaks have disappeared as presented in Fig. 6h. Instead, a peak possibly related to carbonates derivative could be observed. There have been also some changes on the C 1s spectra of GNP8L as can be seen in Fig. 6j, but the shape of spectra between the reference state and the cycled states with different charge rates remained consistent. This finding suggests the enhanced chemical stability against the electrode dissolution into electrolyte during charge-discharge, by the stacked graphene.

4. Conclusion

This study has demonstrated, for the first time, the intriguing capability of the stacked-graphene design (8 layers of graphene basal planes) as an artificial solid interphase layer (SEI) for lithium-ion batteries. Lithium-ion diffusion through the stacked-graphene layers (basal planes) is believed to be significantly suppressed by the physical barrier offered by the stacked-graphene design. Surprisingly, the cell (GNP8L) with the multi layers of stacked-graphene grown by CVD method has displayed a similar level of the battery capacity as NMC111 at slow rate regime in spite of its high lithium-ion migration barrier. Moreover, GNP8L has revealed a better charge capacity and rate capability at rapid charge rates. The magnetic measurements

prove the effective Li^+ intercalation into the stacked layers. Therefore, we propose that the lithium-ions migrate through the defect sites and grain boundaries benefit from the clap-net design of the stacked-graphene enabling a unique structure for efficient electron transport, protecting the active material inside. In both cases, the stacked-graphene cells have presented stable SEI formation under different charge rates bias. It also effectively maintains the local atomic environments of the Mn-O, Co-O, and Ni-O during Li^+ (de)intercalation. The rate kinetics investigation into the formation of SEI layers at the electrode/electrolyte interface not only proves the superior stability of the stacked-graphene system, but also confirms the rate-dependent intercalation mechanism. Our findings shed light on developing electrode materials with enhanced stability, particularly devoted to fast charging applications.

Acknowledgements

This work was supported by funding from the Energy Materials and Surface Sciences Unit of the Okinawa Institute of Science and Technology Graduate University, the OIST R&D Cluster Research Program, and the OIST Proof of Concept (POC) Program.

References

- [1] M. Armand, J.M. Tarascon, Building better batteries, *Nature*. 451 (2008) 652–657.
- [2] J.-M. Tarascon, M. Armand, Issues and challenges facing rechargeable lithium batteries, *Nature*. 414 (2001) 359–367.
- [3] R. Malik, F. Zhou, G. Ceder, Kinetics of non-equilibrium lithium incorporation in LiFePO_4 , *Nat. Mater.* 10 (2011) 587–590.
- [4] K. Mizushima, P.C. Jones, P.J. Wiseman, J.B. Goodenough, Li_xCoO_2 ($x < 0 < 1$): A new cathode material for batteries of high energy density, *Mater. Res. Bull.* 15 (1980) 783–789.
- [5] B. Dunn, H. Kamath, J.M. Tarascon, Electrical energy storage for the grid: A battery of choices, *Science* (80-.). 334 (2011) 928–935.
- [6] J.B. Goodenough, Y. Kim, Challenges for rechargeable Li batteries, *Chem. Mater.* 22 (2010) 587–603.
- [7] E. Solid, S. Ionics, J. Goodenough, Design considerations, *Solid State Ionics*. 69 (1994) 184–198.
- [8] C.M. Julien, A. Mauger, K. Zaghbi, H. Groult, E. Storage, Comparative Issues of Cathode Materials for Li-Ion Batteries, *Inorganics*. (2014) 132–154.
- [9] N. Nitta, F. Wu, J.T. Lee, G. Yushin, Li-ion battery materials: present and future, *Mater. Today*. 18 (2014) 252–264.
- [10] A. Kraytsberg, Y. Ein-Eli, A. Kraytsberg, Y. Ein-Eli, Higher, stronger, better ... A review of 5 volt cathode materials for advanced lithium-ion batteries, *Adv. Energy Mater.* 2 (2012) 922–939.
- [11] C.M. Julien, A. Mauger, Review of 5-V electrodes for Li-ion batteries: Status and trends, 2013.
- [12] P. He, H. Yu, D. Li, H. Zhou, Layered lithium transition metal oxide cathodes towards high energy lithium-ion batteries, *J. Mater. Chem.* 22 (2012) 3680.
- [13] F. Weill, N. Tran, L. Croguennec, C. Delmas, Cation ordering in the layered

- $\text{Li}_{1+x}(\text{Ni}_{0.425}\text{Mn}_{0.425}\text{Co}_{0.15})_{1-x}\text{O}_2$ materials ($x=0$ and 0.12), *J. Power Sources*. 172 (2007) 893–900.
- [14] A.N. Mansour, L. Croguennec, C. Delmas, A Unique Structure of Ni(III) in $\text{LiNi}_{0.3}\text{Co}_{0.7}\text{O}_2$ Without Jahn-Teller Distortion, *Electrochem. Solid-State Lett.* 8 (2005) A544.
- [15] M.M. Thackeray, S.-H. Kang, C.S. Johnson, J.T. Vaughey, R. Benedek, S. a. Hackney, Li_2MnO_3 -stabilized LiMO_2 ($M = \text{Mn, Ni, Co}$) electrodes for lithium-ion batteries, *J. Mater. Chem.* 17 (2007) 3112.
- [16] C.S. Johnson, J.S. Kim, C. Lefief, N. Li, J.T. Vaughey, M.M. Thackeray, The significance of the Li_2MnO_3 component in “composite” $x\text{Li}_2\text{MnO}_3 \cdot (1-x)\text{LiMn}_{0.5}\text{Ni}_{0.5}\text{O}_2$ electrodes, *Electrochem. Commun.* 6 (2004) 1085–1091.
- [17] M.M. Thackeray, S.-H. Kang, C.S. Johnson, J.T. Vaughey, S.A. Hackney, Comments on the structural complexity of lithium-rich $\text{Li}_{1+x}\text{M}_{1-x}\text{O}_2$ electrodes ($M = \text{Mn, Ni, Co}$) for lithium batteries, *Electrochem. Commun.* 8 (2006) 1531–1538.
- [18] D. Kim, G. Sandi, J.R. Croy, K.G. Gallagher, S.-H. Kang, E. Lee, M.D. Slater, C.S. Johnson, M.M. Thackeray, Composite “Layered-Layered-Spinel” Cathode Structures for Lithium-Ion Batteries, *J. Electrochem. Soc.* 160 (2012) A31–A38.
- [19] Z. Li, N.A. Chernova, J. Feng, S. Upreti, F. Omenya, M.S. Whittingham, Stability and Rate Capability of Al Substituted Lithium-Rich High-Manganese Content Oxide Materials for Li-Ion Batteries, *J. Electrochem. Soc.* 159 (2012) A116.
- [20] Q.-Q. Qiao, L. Qin, G.-R. Li, Y.-L. Wang, X.-P. Gao, Sn-stabilized Li-rich layered $\text{Li}(\text{Li}_{0.17}\text{Ni}_{0.25}\text{Mn}_{0.58})\text{O}_2$ oxide as a cathode for advanced lithium-ion batteries, *J. Mater. Chem. A* 3 (2015) 17627–17634.
- [21] T.R. Penki, D. Shanmugasundaram, B. Kishore, A. V. Jeyaseelan, A.K. Subramani, N. Munichandraiah, Composite of Li-Rich Mn, Ni and Fe Oxides as Positive Electrode Materials for Li-Ion Battery, *J. Electrochem. Soc.* 163 (2016) A1493–A1502.
- [22] M.S. Whittingham, Lithium batteries and cathode materials., *Chem. Rev.* 104 (2004) 4271–301.
- [23] J. Vetter, P. Novák, M.R. Wagner, C. Veit, K.-C. Möller, J.O. Besenhard, M. Winter, M. Wohlfahrt-Mehrens, C. Vogler, A. Hammouche, Ageing mechanisms in lithium-ion batteries, *J. Power Sources*. 147 (2005) 269–281.
- [24] M. Gauthier, T.J. Carney, A. Grimaud, L. Giordano, N. Pour, H.-H. Chang, D.P. Fenning, S.F. Lux, O. Paschos, C. Bauer, F. Maglia, S. Lupart, P. Lamp, Y. Shao-Horn, The Electrode-Electrolyte Interface in Li-ion Batteries: Current Understanding and New Insights, *J. Phys. Chem. Lett.* (2015) acs.jpcclett.5b01727.
- [25] E. Peled, Advanced Model for Solid Electrolyte Interphase Electrodes in Liquid and Polymer Electrolytes, *J. Electrochem. Soc.* 144 (1997) L208.
- [26] K. Kanamura, H. Tamura, Z. Takehara, XPS analysis of a lithium surface immersed in propylene carbonate solution containing various salts, *J. Electroanal. Chem.* 333 (1992) 127–142.
- [27] D. Aurbach, Y. Gofer, M. Ben-Zion, P. Aped, The behaviour of lithium electrodes in propylene and ethylene carbonate: The major factors that influence Li cycling efficiency, *J. Electroanal. Chem.* 339 (1992) 451–471.
- [28] D. Aurbach, M.L. Daroux, P.W. Faguy, E. Yeager, Identification of Surface Films Formed on Lithium in Propylene Carbonate Solutions, *J. Electrochem. Soc.* 134 (1987) 1611.
- [29] N.A. Kaskhedikar, J. Maier, Lithium Storage in Carbon Nanostructures, *Adv. Mater.* 21 (2009) 2664–2680.
- [30] F.-Y. Su, Y.-B. He, B. Li, X.-C. Chen, C.-H. You, W. Wei, W. Lv, Q.-H. Yang, F. Kang, Could graphene construct an effective conducting network in a high-power lithium ion battery?, *Nano Energy*. 1 (2012) 429–439.
- [31] M. Liang, L. Zhi, Graphene-based electrode materials for rechargeable lithium batteries, *J. Mater. Chem.* 19 (2009) 5871.
- [32] R. Mukherjee, A.V. Thomas, A. Krishnamurthy, N. Koratkar, Photothermally Reduced Graphene as High-Power Anodes for Lithium-Ion Batteries, *ACS Nano*. 6 (2012) 7867–7878.

- [33] Z.-S. Wu, G. Zhou, L.-C. Yin, W. Ren, F. Li, H.-M. Cheng, Graphene/metal oxide composite electrode materials for energy storage, *Nano Energy*. 1 (2012) 107–131.
- [34] R. Raccichini, A. Varzi, S. Passerini, B. Scrosati, The role of graphene for electrochemical energy storage., *Nat. Mater.* 14 (2015) 271–9.
- [35] L. Jaber-Ansari, K.P. Puntambekar, S. Kim, M. Aykol, L. Luo, J. Wu, B.D. Myers, H. Iddir, J.T. Russell, S.J. Saldaña, R. Kumar, M.M. Thackeray, L.A. Curtiss, V.P. Dravid, C. Wolverton, M.C. Hersam, Suppressing Manganese Dissolution from Lithium Manganese Oxide Spinel Cathodes with Single-Layer Graphene, *Adv. Energy Mater.* 5 (2015) 1500646.
- [36] J. Zhu, D. Yang, Z. Yin, Q. Yan, H. Zhang, Graphene and Graphene-Based Materials for Energy Storage Applications, *Small*. 10 (2014) 3480–3498.
- [37] S. Chattopadhyay, A.L. Lipson, H.J. Karmel, J.D. Emery, T.T. Fister, P.A. Fenter, M.C. Hersam, M.J. Bedzyk, In Situ X-ray Study of the Solid Electrolyte Interphase (SEI) Formation on Graphene as a Model Li-ion Battery Anode, *Chem. Mater.* 24 (2012) 3038–3043.
- [38] N. Li, Y. Yin, C. Yang, Y. Guo, An Artificial Solid Electrolyte Interphase Layer for Stable Lithium Metal Anodes, *Adv. Mater.* (2016) 1853–1858.
- [39] S. Menkin, D. Golodnitsky, E. Peled, Artificial solid-electrolyte interphase (SEI) for improved cycleability and safety of lithium-ion cells for EV applications, *Electrochem. Commun.* 11 (2009) 1789–1791.
- [40] J. Zhao, Z. Lu, H. Wang, W. Liu, H.-W. Lee, K. Yan, D. Zhuo, D. Lin, N. Liu, Y. Cui, Artificial Solid Electrolyte Interphase-Protected Li_xSi Nanoparticles: An Efficient and Stable Prelithiation Reagent for Lithium-Ion Batteries., *J. Am. Chem. Soc.* 137 (2015) 8372–5.
- [41] J.R. Dahn, Phase diagram of Li_xC_6 , *Phys. Rev. B.* 44 (1991) 9170–9177.
- [42] M. Winter, J.O. Besenhard, M.E. Spahr, P. Novák, Insertion Electrode Materials for Rechargeable Lithium Batteries, *Adv. Mater.* 10 (1998) 725–763.
- [43] A.F. Morpurgo, Ten years of Nature Physics: The ABC of 2D materials, *Nat. Phys.* 11 (2015) 625–626.
- [44] F. Yao, Q. Ta, M. Lee, J. Chae, Y. Sheem, Diffusion Mechanism of Lithium Ion through Basal Plane of Layered Graphene, *J. Am. Chem. Soc.* 134 (2012).
- [45] J. Hui, M. Burgess, J. Zhang, J. Rodríguez-López, Layer Number Dependence of Li^+ Intercalation on Few-Layer Graphene and Electrochemical Imaging of Its Solid-Electrolyte Interphase Evolution, *ACS Nano*. 10 (2016) 4248–4257.
- [46] K. Persson, V.A. Sethuraman, L.J. Hardwick, Y. Hinuma, Y.S. Meng, A. van der Ven, V. Srinivasan, R. Kostecki, G. Ceder, Lithium Diffusion in Graphitic Carbon, *J. Phys. Chem. Lett.* 1 (2010) 1176–1180.
- [47] Z. Jiang, B. Pei, A. Manthiram, Randomly stacked holey graphene anodes for lithium ion batteries with enhanced electrochemical performance, *J. Mater. Chem. A*. 1 (2013) 7775.
- [48] M.V. Kamalakar, C. Groenveld, A. Dankert, S.P. Dash, Long distance spin communication in chemical vapour deposited graphene, *Nat. Commun.* 6 (2015) 6766.
- [49] J. Wang, Y.K. Chen-Wiegart, J. Wang, In operando tracking phase transformation evolution of lithium iron phosphate with hard X-ray microscopy., *Nat. Commun.* 5 (2014) 4570.
- [50] G. Dutta, A. Manthiram, J.B. Goodenough, J.-C. Grenier, Chemical synthesis and properties of $\text{Li}_{1-\delta-x}\text{Ni}_{1+\delta}\text{O}_2$ and $\text{Li}[\text{Ni}_2]\text{O}_4$, *J. Solid State Chem.* 96 (1992) 123–131.
- [51] D. Mohanty, A.S. Sefat, S. Kalnaus, J. Li, R. a. Meisner, E.A. Payzant, D.P. Abraham, D.L. Wood, C. Daniel, Investigating phase transformation in the $\text{Li}_{1.2}\text{Co}_{0.1}\text{Mn}_{0.55}\text{Ni}_{0.15}\text{O}_2$ lithium-ion battery cathode during high-voltage hold (4.5 V) via magnetic, X-ray diffraction and electron microscopy studies, *J. Mater. Chem. A*. 1 (2013) 6249.
- [52] K. Ben-Kamel, N. Amdouni, A. Mauger, C.M. Julien, Study of the local structure of $\text{LiNi}_{0.33+\delta}\text{Mn}_{0.33+\delta}\text{Co}_{0.33-2\delta}\text{O}_2$ ($0.025 \leq \delta \leq 0.075$) oxides, *J. Alloys Compd.* 528 (2012) 91–98.
- [53] N. Tran, L. Croguennec, M. Ménétrier, F. Weill, P. Biensan, C. Jordy, C. Delmas, Mechanisms associated with the “plateau” observed at high voltage for the overlithiated $\text{Li}_{1.12}(\text{Ni}_{0.425}\text{Mn}_{0.425}\text{Co}_{0.15})_{0.88}\text{O}_2$ system, *Chem. Mater.* 20 (2008) 4815–4825.

- [54] O. V. Yazyev, L. Helm, Defect-induced magnetism in graphene, *Phys. Rev. B.* 75 (2007) 1–5.
- [55] C.N.R. Rao, H.S.S.R. Matte, K.S. Subrahmanyam, U. Maitra, Unusual magnetic properties of graphene and related materials, *Chem. Sci.* 3 (2012) 45.
- [56] W. Han, R.K. Kawakami, M. Gmitra, J. Fabian, Graphene spintronics, *Nat. Nanotechnol.* 9 (2014) 794–807.
- [57] R.R. Nair, M. Sepioni, I. Tsai, O. Lehtinen, J. Keinonen, A. V. Krasheninnikov, T. Thomson, A.K. Geim, I. V. Grigorieva, Spin-half paramagnetism in graphene induced by point defects, *Nat. Phys.* 8 (2012) 199–202.
- [58] L. Jaber-Ansari, K.P. Puntambekar, H. Tavassol, H. Yildirim, A. Kinaci, R. Kumar, S.J. Saldaña, A.A. Gewirth, J.P. Greeley, M.K.Y. Chan, M.C. Hersam, Defect Evolution in Graphene upon Electrochemical Lithiation, *ACS Appl. Mater. Interfaces.* 6 (2014) 17626–17636.
- [59] X. Li, W. Cai, J. An, S. Kim, J. Nah, D. Yang, R. Piner, A. Velamakanni, I. Jung, E. Tutuc, S.K. Banerjee, L. Colombo, R.S. Ruoff, Large-Area Synthesis of High-Quality and Uniform Graphene Films on Copper Foils, *Science* (80-.). 324 (2009).
- [60] D. Mohanty, S. Kalnaus, R. a. Meisner, K.J. Rhodes, J. Li, E.A. Payzant, D.L. Wood, C. Daniel, Structural transformation of a lithium-rich $\text{Li}_{1.2}\text{Co}_{0.1}\text{Mn}_{0.55}\text{Ni}_{0.15}\text{O}_2$ cathode during high voltage cycling resolved by in situ X-ray diffraction, *J. Power Sources.* 229 (2013) 239–248.
- [61] T. Ohzuku, Solid-State Redox Reactions of LiCoO_2 (R3m) for 4 Volt Secondary Lithium Cells, *J. Electrochem. Soc.* 141 (1994) 2972.
- [62] T. Ohzuku, Electrochemistry and Structural Chemistry of LiNiO_2 (R3m) for 4 Volt Secondary Lithium Cells, *J. Electrochem. Soc.* 140 (1993) 1862.
- [63] A. Rougier, P. Gravereau, C. Delmas, Optimization of the Composition of the $\text{Li}_{1-z}\text{Ni}_{1+z}\text{O}_2$ Electrode Materials: Structural, Magnetic, and Electrochemical Studies, *J. Electrochem. Soc.* 143 (1996) 1168–1175.
- [64] A.C. Ferrari, J. Robertson, Interpretation of Raman spectra of disordered and amorphous carbon, *Phys. Rev. B.* 61 (2000) 14095–14107.
- [65] A.C. Ferrari, Raman spectroscopy of graphene and graphite: Disorder, electron–phonon coupling, doping and nonadiabatic effects, *Solid State Commun.* 143 (2007) 47–57.
- [66] R. Baddour-Hadjean, J.-P. Pereira-Ramos, Raman Microspectrometry Applied to the Study of Electrode Materials for Lithium Batteries, *Chem. Rev.* 110 (2010) 1278–1319.
- [67] M.M. Doeff, Y. Hu, F. McLarnon, R. Kostecki, Effect of Surface Carbon Structure on the Electrochemical Performance of LiFePO_4 , *Electrochem. Solid-State Lett.* 6 (2003) A207.
- [68] N. Tran, L. Croguennec, C. Labrugère, C. Jordy, P. Biensan, C. Delmas, Layered $\text{Li}_{1+x}(\text{Ni}_{0.425}\text{Mn}_{0.425}\text{Co}_{0.15})_{1-x}\text{O}_2$ Positive Electrode Materials for Lithium-Ion Batteries, *J. Electrochem. Soc.* 153 (2006) A261.
- [69] B.J. Hwang, Y.W. Tsai, D. Carlier, G. Ceder, A Combined Computational/Experimental Study on $\text{LiNi}_{1/3}\text{Co}_{1/3}\text{Mn}_{1/3}\text{O}_2$, *Chem. Mater.* 15 (2003) 3676–3682.
- [70] R. Prasad, R. Benedek, A. Kropf, C. Johnson, A. Robertson, P. Bruce, M. Thackeray, Divalent-dopant criterion for the suppression of Jahn-Teller distortion in Mn oxides: First-principles calculations and x-ray absorption spectroscopy measurements for Co in LiMnO_2 , *Phys. Rev. B.* 68 (2003) 12101.
- [71] Z.F. Huang, F. Du, C.Z. Wang, D.P. Wang, G. Chen, Low-spin Mn^{3+} ion in rhombohedral LiMnO_2 predicted by first-principles calculations, *Phys. Rev. B - Condens. Matter Mater. Phys.* 75 (2007) 54411.
- [72] Z.-D. Huang, X.-M. Liu, S.-W. Oh, B. Zhang, P.-C. Ma, J.-K. Kim, Microscopically porous, interconnected single crystal $\text{LiNi}_{1/3}\text{Co}_{1/3}\text{Mn}_{1/3}\text{O}_2$ cathode material for Lithium ion batteries, *J. Mater. Chem.* 21 (2011) 10777.
- [73] T. Eriksson, A.M. Andersson, A.G. Bishop, C. Gejke, T. Gustafsson, J.O. Thomas, Surface Analysis of LiMn_2O_4 Electrodes in Carbonate-Based Electrolytes, *J. Electrochem. Soc.* 149 (2002) A69.
- [74] S.F. Lux, I.T. Lucas, E. Pollak, S. Passerini, M. Winter, R. Kostecki, The mechanism of HF formation in LiPF_6 based organic carbonate electrolytes, 2012.

- [75] W. Li, B.L. Lucht, Lithium-Ion Batteries: Thermal Reactions of Electrolyte with the Surface of Metal Oxide Cathode Particles, *J. Electrochem. Soc.* 153 (2006) A1617.
- [76] S.K. Martha, H. Sclar, Z. Szmuk Framowitz, D. Kovacheva, N. Saliyski, Y. Gofer, P. Sharon, E. Golik, B. Markovsky, D. Aurbach, A comparative study of electrodes comprising nanometric and submicron particles of $\text{LiNi}_{0.50}\text{Mn}_{0.50}\text{O}_2$, $\text{LiNi}_{0.33}\text{Mn}_{0.33}\text{Co}_{0.33}\text{O}_2$, and $\text{LiNi}_{0.40}\text{Mn}_{0.40}\text{Co}_{0.20}$, *J. Power Sources.* 189 (2009) 248–255.
- [77] J.R. González, R. Menéndez, R. Alcántara, F. Nacimiento, J.L. Tirado, E. Zhecheva, R. Stoyanova, High-intensity ultrasonication as a way to prepare graphene/amorphous iron oxyhydroxide hybrid electrode with high capacity in lithium battery, *Ultrason. Sonochem.* 24 (2015) 238–246.
- [78] Q. Li, C. Wang, Q. Li, R. Che, The role of graphene in nano-layered structure and long-term cycling stability of $\text{Mn}_x\text{Co}_y\text{Ni}_z\text{CO}_3$ as an anode material for lithium-ion batteries, *RSC Adv.* 6 (2016) 105252–105261.
- [79] R. Armstrong, M. Holzapfel, P. Novák, C.S. Johnson, S.H. Kang, M.M. Thackeray, P.G. Bruce, Demonstrating oxygen loss and associated structural reorganization in the lithium battery cathode $\text{Li}[\text{Ni}_{0.2}\text{Li}_{0.2}\text{Mn}_{0.6}]\text{O}_2$, *J. Am. Chem. Soc.* 128 (2006) 8694–8698.
- [80] Z. Lu, J.R. Dahn, Understanding the Anomalous Capacity of $\text{Li}/\text{Li}[\text{Ni}_x\text{Li}_{(1/3-2x/3)}]\text{Mn}_{(2/3-x/3)}\text{O}_2$ Cells Using In Situ X-Ray Diffraction and Electrochemical Studies, *J. Electrochem. Soc.* 149 (2002) A815.
- [81] A.M. Andersson, D.P. Abraham, R. Haasch, S. MacLaren, J. Liu, K. Amine, Surface Characterization of Electrodes from High Power Lithium-Ion Batteries, *J. Electrochem. Soc.* 149 (2002) A1358.
- [82] T. Eriksson, A.M. Andersson, C. Gejke, T. Gustafsson, J.O. Thomas, Influence of temperature on the interface chemistry of $\text{Li}_x\text{Mn}_2\text{O}_4$ electrodes, *Langmuir.* 18 (2002) 3609–3619.
- [83] K. Edström, T. Gustafsson, J.O. Thomas, The cathode–electrolyte interface in the Li-ion battery, *Electrochim. Acta.* 50 (2004) 397–403.
- [84] D. Bar-Tow, E. Peled, L. Burstein, A Study of Highly Oriented Pyrolytic Graphite as a Model for the Graphite Anode in Li-Ion Batteries, *J. Electrochem. Soc.* 146 (1999) 824.
- [85] N.N. Sinha, N. Munichandraiah, Synthesis and Characterization of Carbon-Coated $\text{LiNi}_{1/3}\text{Co}_{1/3}\text{Mn}_{1/3}\text{O}_2$ in a Single Step by an Inverse Microemulsion Route, *ACS Appl. Mater. Interfaces.* 1 (2009) 1241–1249.
- [86] M. Xu, L. Zhou, Y. Dong, Y. Chen, J. Demeaux, A.D. MacIntosh, A. Garsuch, B.L. Lucht, Development of novel lithium borate additives for designed surface modification of high voltage $\text{LiNi}_{0.5}\text{Mn}_{1.5}\text{O}_4$ cathodes, *Energy Environ. Sci.* 9 (2016) 1308–1319.